International Symposium
On Turbulence and Shear Flow
Phenomena (TSFP-9)
June 30 - July 3, 2015 *Melbourne, Australia*

CHARACTERISTICS OF THE ENTRAINMENT VELOCITY IN A DEVELOPING WAKE

Jimmy Philip
Department of Mechanical Engineering
The University of Melbourne
Parkville - 3010, VIC, Australia.
jimmyp@unimelb.edu.au

Iván Bermejo-Moreno
Department of Aerospace and Mechanical Engineering,
University of Southern California,
Los Angeles, California 90089-1453, USA.
bermejom@usc.edu

Daniel Chung
Department of Mechanical Engineering,
The University of Melbourne
Parkville - 3010, VIC, Australia.
dchung@unimelb.edu.au

Ivan Marusic
Department of Mechanical Engineering,
The University of Melbourne
Parkville - 3010, VIC, Australia.
imarusic@unimelb.edu.au

ABSTRACT

Characteristics of enstrophy generation and entrainment velocity at the turbulent non-turbulent interface of a temporally evolving wake are studied using Direct Numerical Simulations (DNS), starting from the time instance when the instabilities develop to a fully turbulent state. Results reveal the dominant role of viscous effects compared to the production of enstrophy at the interface at all time instances, although Kolmogorov scaling is found not to apply. The entrainment velocity v_n is dominated by a balance of viscous diffusion and dissipation of enstrophy, and the pdf of v_n shows large positive tails in fully turbulent regimes which are absent during the initial development of the wake. Many salient features of the entrainment velocity can also be explained by the analytically tractable solution of a laminar wake. Furthermore, the propagation velocity of the interface seems to be dictated by the local fluid velocity for all time instances. Finally, we introduce the dependence of entrainment velocity on the local geometry through the geometric parameters of 'curvedness' and 'shape index'. It is found that TNTI dominated by concave regions with radii of curvature similar to Taylor microscale, with entrainment happening mostly through these concave lower curvedness or flatter regions.

INTRODUCTION AND OBJECTIVES

Over the past few years there has been an increased number of investigations on characteristics of entrainment at the turbulent non-turbulent interface (TNTI) of turbulent shear flows, such as wakes, jets and boundary layers (e.g, Bisset *et al.*, 2002; Westerweel *et al.*, 2005; Holzner & Lüthi, 2011; Philip *et al.*, 2014; Chauhan *et al.*, 2014; da Silva *et al.*, 2014*a*). There are many interesting features that characterise the TNTI, and one important feature is the entrainment velocity - the difference between the propagation of the TNTI and the fluid velocity. Entrainment velocity has been studied for example by Wolf *et al.* (2012) experimentally for the case of a turbulent jet. Here we intend to (i) examine the various characteristics of entrainment velocity in the 'developing' and the 'fully turbulent' regimes of a temporally evolving wake using DNS. After corroborating some of the recent findings, we show features of the viscous and inviscid components of entrainment velocity at the TNTI as the wake develops in time, as well as the strong correlation of the propagation velocity of TNTI with the local fluid velocity. (ii) Quantify the geometric features of the TNTI and their relation to the entrainment velocity.

NUMERICAL SIMULATIONS

The numerical simulations follow the pseudo-spectral DNS study of da Silva & Pereira (2008). The domain is periodic in all three directions with a size of $L_x \times L_y \times L_z$ = $4 \times 6 \times 4$, with number of points $N_x \times N_y \times N_z$ = $384 \times 576 \times 384$. The Navier-Stokes equations are solved by projecting onto Fourier modes where the nonlinear terms are treated explicitly and viscous terms implicitly. The initial condition involves a step velocity profile (c.f. equation 5) along with a random noise of about 8% to induce transition. The Reynolds number (Re) based on the initial centreline velocity (u_0) and width of the velocity profile (L) is 3200. The streamwise, normal and spanwise directions are x, y and z. The temporally evolving wake starts undergoing transition by time of $t \approx 500$ and simulations continues till $t \approx 2500$ before the box effects come into play. Figure 1 shows contours of enstrophy production at four different time instances across a z=constant plane.

CHARACTERISTICS OF ENTRAINMENT VELOCITY

The turbulent non-turbulent interface (TNTI) is defined here using an isosurface of enstrophy, ω^2, where the vorticity $\boldsymbol{\omega} = \nabla \times \mathbf{u}$, and normal to TNTI, $\mathbf{n} = \nabla\omega^2/|\nabla\omega^2|$, see figure 2. The evolution of this isosurface, which is propagating at a velocity, say, $\mathbf{v}^{surf}$ is given by,

$$\frac{\partial \omega^2}{\partial t} + \mathbf{v}^{surf} \cdot (\nabla \omega^2) = 0, \text{ or, } v_n^{surf} = \frac{-1}{|\nabla \omega^2|} \frac{\partial \omega^2}{\partial t}, \quad (1)$$

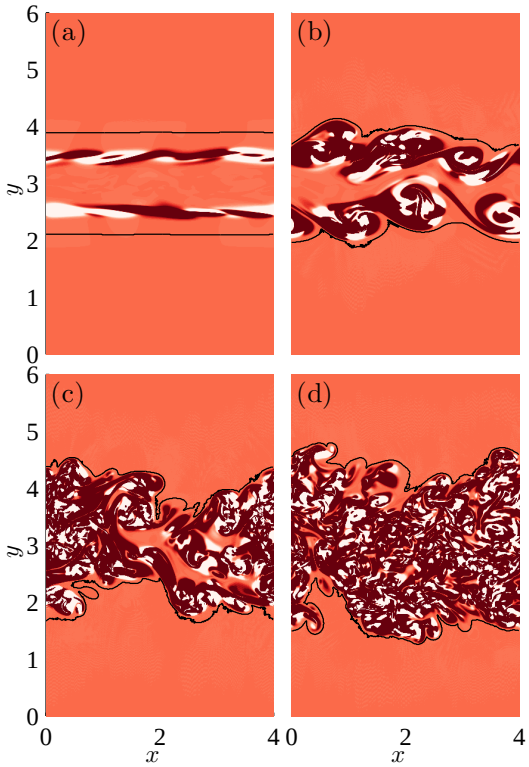

Figure 1. Contours of enstrophy production, $\omega_i\omega_j s_{ij}$ at the time instances, (a) t=500; (b) t=1000; (c) t=1500; (d) t=2000. The scale varies linearly from -1 (light) to 1 (dark). The black lines are the TNTI defined on a threshold on ω^2.

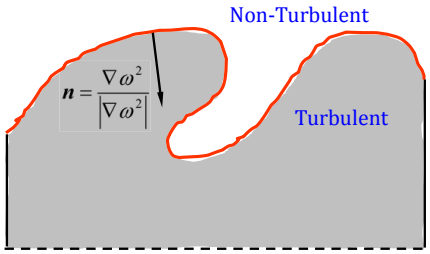

Figure 2. Schematic of TNTI and definition of normal **n**.

where, v_n^{surf} is the magnitude of $\mathbf{v}^{surf}$ in the direction of **n**. The entrainment velocity, $\mathbf{v} = \mathbf{v}^{surf} - \mathbf{u}$, is the relative velocity between the surface propagation and the fluid velocity. Employing the evolution equation for ω^2 and (1), the entrainment velocity normal to **n**, v_n is given by (e.g, Holzner & Lüthi, 2011),

$$v_n = \underbrace{\frac{(-2\omega_i\omega_j s_{ij})}{|\nabla\omega^2|}}_{v_n^{inv}} + \underbrace{\frac{-\nu}{|\nabla\omega^2|}\frac{\partial\omega_i^2}{\partial x_j\partial x_j}}_{v_n^{dif}} + \underbrace{\frac{2\nu}{|\nabla\omega^2|}\left(\frac{\partial\omega_i}{\partial x_j}\right)^2}_{v_n^{dis}}, \tag{2}$$

where, v_n is the sum of the inviscid, v_n^{inv}, and viscous v_n^{vis} entrainment velocities, and the viscous component is further divided into diffusive and dissipative components, $v_n^{vis} = v_n^{dif} + v_n^{dis}$.

The first task at hand is the identification of TNTI defined by a threshold of enstrophy. This is carried out following da Silva *et al.* (2014*b*) by plotting the pdf of $\log(\omega^2)$,

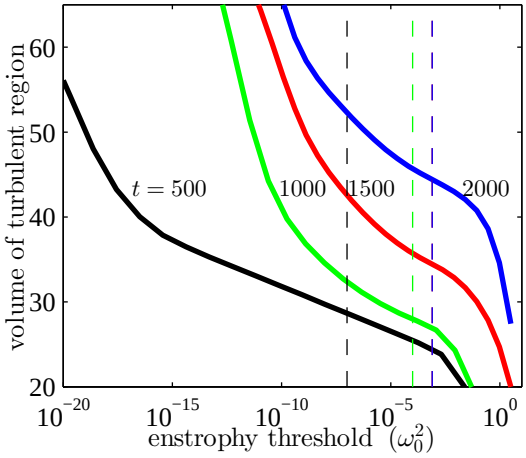

Figure 3. Threshold detection for identifying TNTI at different t. The vertical lines at the threshold levels ω_0^2=10^{-7} (t=500), 10^{-4} (t=1000) and $10^{-3.1}$ (t=1500 and 2000).

which has a bimodal distribution, and locating the minimum between the two peaks. This is similar to identifying the location of inflection point on figure 3, which shows the volume of the turbulent region for four different times of evolution (corresponding to figure 1) on a logarithmic scale as a function of the threshold vorticity ω_0^2. Note that figure 1 shows TNTI identified by this process, which seems reasonable for fully turbulent regimes, however, for lower simulations times, there is still some ambiguity.

It is of interest to understand the behaviour of the terms involved in the production of enstrophy, the inviscid contribution, and the diffusion and dissipation of vorticity, the viscous contribution as a precursor to understanding the entrainment velocity. Figure 4 shows the conditional average of $2\omega_i\omega_j s_{ij}$, $\nu(\partial\omega_i^2)/(\partial x_j\partial x_j)$ and $-2\nu(\partial\omega_i/\partial x_j)^2$ represented by angled brackets $\langle\,\rangle_n$ along the direction normal to the interface, denoted by the local coordinate ζ with its origin at the TNTI and positive towards the turbulent region. The distance ζ and the various terms in the enstrophy equation are normalised by the Kolmogorov length and velocity scales η and u_η, respectively, computed at the center plane of the wake.

Figure 4(a) shows the conditional profiles for t=2000 and figure 4(b) a zoomed in view at the TNTI. The distributions are similar to those found by Taveira *et al.* (2013) where the evolution of enstrophy at TNTI seems to be dominated by the action of two viscous contributions. Figure 4(c) shows the distributions at different times, which are similar to one another qualitatively, however, very different when absolute magnitudes are compared. Note that the magnitudes at different times are multiplied by different factors to be shown on the same figure (see caption). This shows that the magnitudes do not scale on Kolmogorov scales during the development of the wake. It is not surprising that the scaling during transition might be different from the fully developed regime, however, even in the fully turbulent regime we observe the inadequacy of Kolmogorov scaling. In fact, it has been found by da Silva & Taveira (2010) in jets that the Taylor microscale might be a more relevant length scale at TNTI and similar conclusions have been reached by Chauhan *et al.* (2014) for a boundary layer.

The pdf of the entrainment velocities at t=2000 are shown in figure 5(a). It shows that the entrainment veloc-

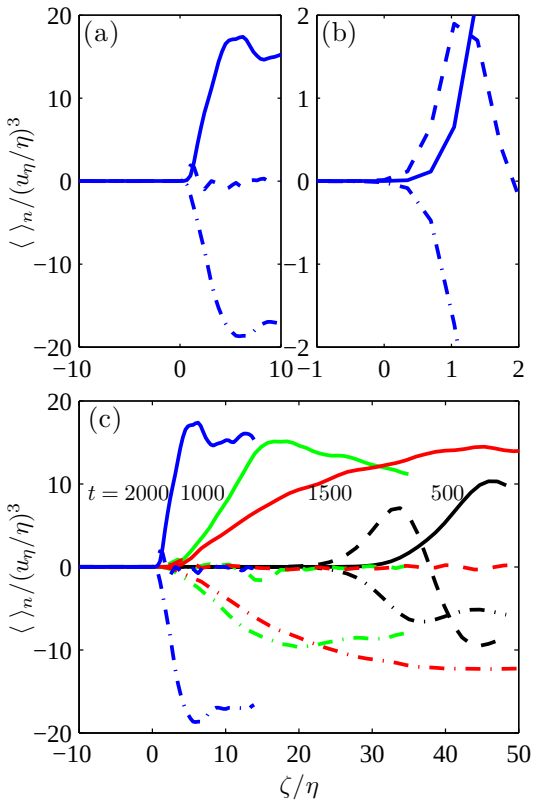

Figure 4. Conditional average of terms in the enstrophy equation across the TNTI. Full lines: $\langle 2\omega_i\omega_j s_{ij}\rangle_n$, dashed lines: $\langle \nu(\partial\omega_i^2)/(\partial x_j\partial x_j)\rangle_n$, dashed dotted lines: $\langle -2\nu(\partial\omega_i/\partial x_j)^2\rangle_n$. (a) t=2000, (b) zoomed in view of (a) close to the TNTI, and (c) for different time instances. Note that in (c) the distributions at t=500, 1000 and 1500 are multiplied by a factor of 10, 5 and 30, respectively, to make it appear on the same figure at par with t=2000.

ity v_n (in thick dashed dotted black line) is dominated by the viscous component v_n^{vis} in agreement with Wolf *et al.* (2012); however, it is interesting to note that diffusive and dissipative parts of the viscous components play opposing roles. These observations become more clear at t=500 shown in figure 5(b), where the pdfs separate from each other distinctively. Here the pdf of v_n^{inv} is close to zero and narrowly distributed, and the pdf of v_n closely follows v_n^{vis}. The pdfs at other time instances corresponding to t=1000 and 1500 follow closely that of t=2000, which can be considered 'fully' turbulent regimes. The distinguishing feature of the fully turbulent regimes are the long positive tails of the pdf of v_n, whereas the peak location is at negative v_n, which is unlike the almost symmetric pdfs at t=500, shown in figure 5(c) where v_n for the four cases are presented.

The pdf at $t = 500$ is peculiar in that the $v_n^{inv} \approx 0$ and $v_n^{dif}/v_n^{dis} \approx -2$. The pdfs at other times do show these features but only mildly. The origin of these features can be explained if we consider the 'entrainment velocity for a laminar wake', which can be treated analytically. This is presented in the Appendix, and suggests the dominance of viscous effects at the TNTI with almost negligible production (also see figure 4b).

Once v_n is calculated the propagation velocity of the

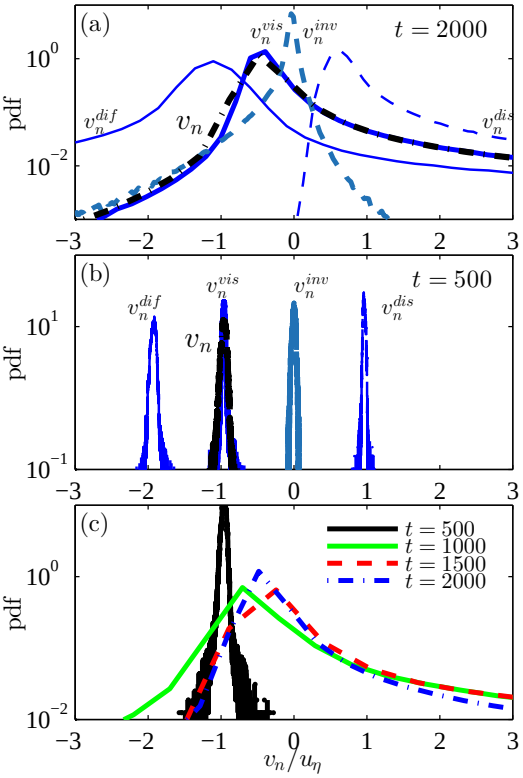

Figure 5. Pdf of the various components of entrainment velocity. (a) t=2000, (b) t=500, and (c) v_n for different t.

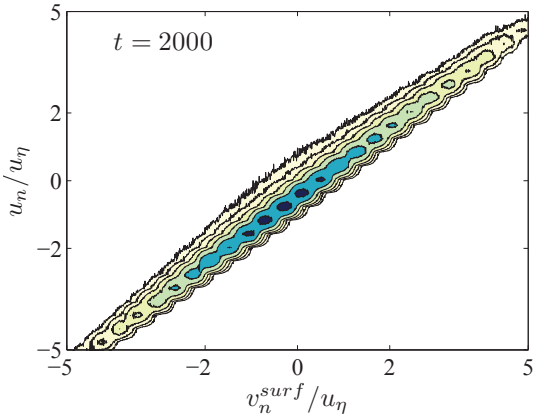

Figure 6. Joint pdf of u_n and v_n^{surf} at t=2000. The contour levels are logarithmical spaced from 10^{-2} to 1 in steps of $10^{0.25}$.

TNTI is found by, $v_n^{surf} = v_n + u_n$, where u_n is fluid velocity at the TNTI along **n**. A joint pdf of v_n^{surf} and u_n normalised by u_η at t=2000 is presented in figure 6. This behaviour is qualitatively similar at other time instances also. The strong correlation between v_n^{surf} and u_n suggests that for most part the interface is simply advected by the fluid velocity. And on occasions where the v_n^{surf} differs from u_n, mostly due to viscous effects, is when the entrainment happens.

GEOMETRIC FEATURES OF THE TNTI AND ITS RELATION TO THE ENTRAINMENT VELOCITY

Figure 7 shows the TNTI on one side of the wake at t=2000 coloured by v_n, illustrating the effect of geometry on entrainment. It is clear that different regions of the interface

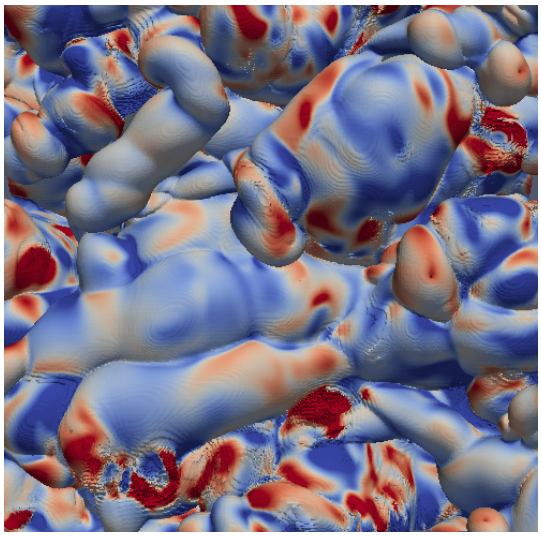

Figure 7. TNTI shown as an isosurface of ω^2 from one side of the wake at t=2000 coloured by v_n/u_η between -0.5 (blue) and +0.5 (red).

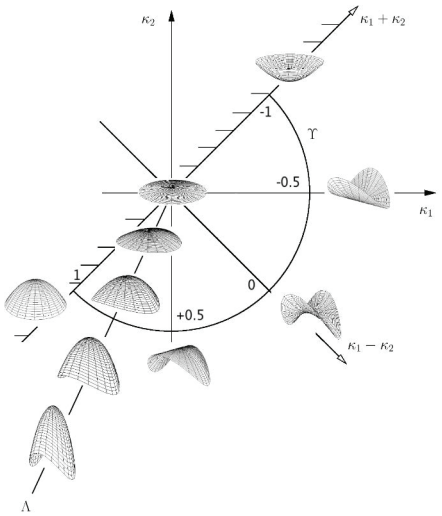

Figure 8. Shape index, Υ, and curvedness, Λ mapped on the plane of principal curvatures, $\{\kappa_1, \kappa_2\}$.

preferentially allow entrainment or detrainment depending on the local geometrical features.

The geometry of the TNTI is characterised using the shape index, Υ, and curvedness, Λ, defined as (e.g., Koenderink & van Doorn (1992) and Bermejo-Moreno & Pullin (2008)):

$$\Upsilon := -\frac{2}{\pi}\tan^{-1}\left(\frac{\kappa_1+\kappa_2}{\kappa_1-\kappa_2}\right), \text{ and } \Lambda := \sqrt{\frac{\kappa_1^2+\kappa_2^2}{2}}, \quad (3)$$

where, κ_1 and κ_2 are the principle curvatures calculated at each point on the TNTI. Figure 8 shows the shapes corresponding to different values of Υ and Λ. The shape index ($\Upsilon \in [-1,1]$) represents the local shape of the surface, given by its absolute value, with its sign distinguishing concave (negative) from convex (positive) shapes. The curvedness ($\Lambda \geq 0$) has dimensions of $length^{-1}$ and is the inverse of a representative radius of curvature of the surface at each point. The curvedness is zero for locally planar surface and is larger for increasingly curved surfaces.

Once the differential-geometry properties, Υ and Λ, are mapped at each point of the TNTI, a joint probability density function, $P(\Upsilon,\Lambda)$, based on area coverage in terms of those two geometric properties is calculated. This joint PDF is shown in figure 9 for $t = 2000$. $P(\Upsilon,\Lambda)$ peaks (in dark red) at a value of the shape index around -0.5, which corresponds to a predominance of trough (parabolic) points (see figure 8), and a curvedness of approximately $7.2/L$, corresponding to a radius of curvature of $0.14L$. It is interesting to note that the Taylor microscale (based on the centre plane) is also about $0.14L$, which suggests that the average vortices along the TNTI are of the order of Taylor microscale, in accordance with da Silva & Taveira (2010) in jets and Chauhan *et al.* (2014) in a boundary layer (also see figure 4a and the related comments).

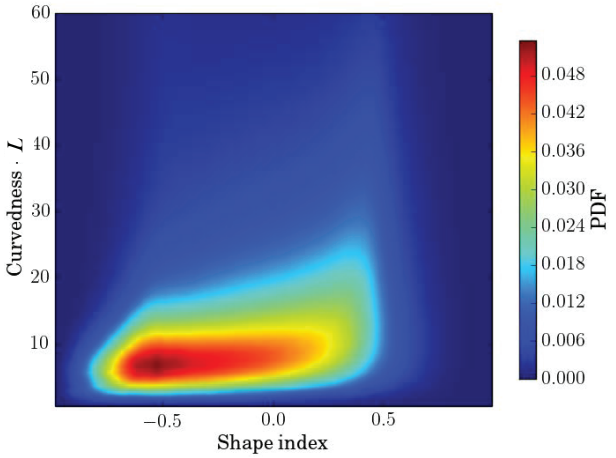

Figure 9. Area-based joint probability density function in terms of shape index and curvedness mapped onto the TNTI at $t = 2000$.

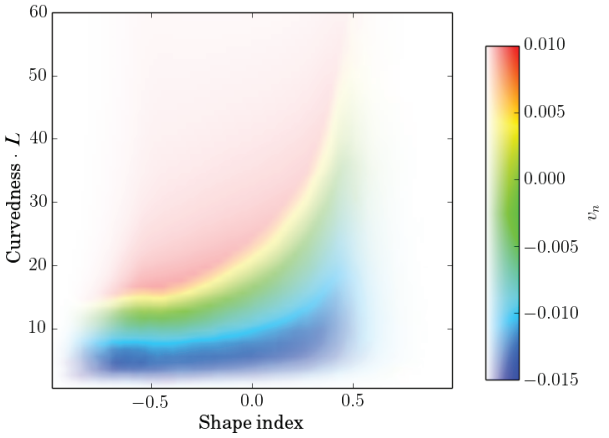

Figure 10. Conditional average of v_n at $t = 2000$ (hue, from blue to red) combined with the $P(\Upsilon,\Lambda)$ (saturation, with white corresponding to $P = 0$).

Near the peak of $\Lambda \approx -0.5$, high values of $P(\Upsilon,\Lambda)$ are still present and extend, in particular, down to lower values of the shape index ($\Upsilon \in [-0.8,-0.5]$) and decreasing curvedness, which correspond to larger trough-like (concave) regions of the TNTI. For larger values of the shape index, $P(\Upsilon,\Lambda)$ extends over broader ranges of curvedness through the different saddle point configurations up to the ridge shape ($\Upsilon \approx 0.5$). Thus, convex regions of the TNTI show on average shorter radii of curvature. These are the valleys between the large bulges shown in figure 7.

Besides the purely geometrical analysis of the TNTI,

its physics can also be explored in relation with the local geometry of the interface by computing the area-based conditional average of the signed local entrainment velocity conditioned on the shape index and curvedness, $E[v_n|\Upsilon,\Lambda]$. Figure 10 represents that conditional average of v_n combined with the information contained in $P(\Upsilon,\Lambda)$ to account for the fact that not all values of the $\Upsilon\Lambda$ plane are equally probable in the TNTI: this is accomplished by using a hue scale to represent $E[v_n|\Upsilon,\Lambda]$ (from blue to red) and a saturation filter to represent the $P(\Upsilon,\Lambda)$, masking (toward white) regions of the $\Upsilon\Lambda$ plane with low probability density $P(\Upsilon,\Lambda)$.

At each value of the shape index, v_n monotonically increases with curvedness (corresponding to the large positive tails in the pdfs of figure 5c), for the range of relevant regions in the $\Upsilon\Lambda$ plane. Flatter regions of the interface appear dominated by negative entrainment velocities. The curvedness at which the entrainment velocity becomes positive also increases nearly monotonically with the shape index. Thus, entrainment of fluid from non-turbulent flow into the turbulent wake occurs at lower curvedness for concave regions of the interface than for convex shapes.

CONCLUSIONS

For a temporally evolving wake the conditional profiles of the vorticity production, diffusion and dissipation across the TNTI reveal a balance of diffusion and dissipation close to the TNTI whereas the usual balance of production and dissipation is observed deep inside the turbulent region. Qualitatively, the different evolution instances show similar trends, however, their scaling with Kolmogorov length and velocity scale over the development is doubtful, and an appropriate scaling requires further study.

The entrainment velocity is dominated by viscous diffusive and dissipative contributions, and show large positive tails in the fully turbulent regimes, which are absent for the initial part of the wake development where the pdf tails are narrower. Interestingly, the laminar solution of the wake shows the ratio of the diffusive and dissipative components of the entrainment velocities to be approximately -2, which has similarities to the observations in the fully turbulent wake. Also, the exactly zero contribution of the inviscid component of entrainment velocity in a laminar flow is similar to the negligible (though non-zero) contribution of inviscid component in the turbulent case. Furthermore, the propagation of the TNTI is found to be mostly to due to the fluid motions, rather than due to entrainment.

It is observed that the geometry of the TNTI has a strong influence over the entrainment. Here we characterise the TNTI geometry using two parameters, 'curvedness' and 'shape index'. The joint pdf of 'curvedness' and 'shape index' for the TNTI shows that, the convex (valley) and concave (bulge) regions of the TNTI have on average shorter and larger radii of curvatures, respectively. Concave trough like regions are predominant on the TNTI and their average radius of curvature has a magnitude similar to the Taylor microscale, suggesting a dominance of eddies of the size of Taylor microscale in the vicinity of the TNTI. When entrainment velocity is conditioned on the geometric parameters, it is found that the entrainment is happening mostly over concave regions (bulges) where the curvedness is less (flatter regions) of the TNTI rather than over the convex (valley) regions.

Presently, one specific threshold is used to identify TNTI. When the threshold is varied (in the manner of van Reeuwijk & Holzner (2014)), the geometric characteristics would vary and the corresponding entrainment velocities. In future it is of interest to understand how the changing geometric characteristics affect the entrainment velocities, which will pave inroads to further understand the role of large scale engulfment and small scale nibbling contributions (e.g, Philip & Marusic, 2012).

Acknowledgements

The authors JP, DC and IM wish to thank the Australian Research Council for the financial support of this work.

APPENDIX: Entrainment velocity for a laminar wake

For the laminar case of a temporally evolving wake (with periodic boundary conditions), the Navier-Stokes equations reduce to a diffusion equation for the streamwise velocity, u:

$$\frac{\partial u}{\partial t} = \nu \frac{\partial^2 u}{\partial^2 y}, \tag{4}$$

with the initial condition,

$$u(y,t=0) = u_0(\mathrm{H}(y+L/2) - \mathrm{H}(y-L/2)), \tag{5}$$

where, u_0 is the initial streamwise velocity amplitude, $\mathrm{H}(x)$ is the Heaviside function such that, $\mathrm{H}(x) = 0$ for $x < 0$ and equal to 1 for $x \geq 0$, and L is spanwise extent of the initial condition. In the DNS simulations $L = 1$, with the maximum spanwise (y) extent being -3 to 3. The solution to equation (4) is the convolution of its Green's function, $1/\sqrt{4\pi\nu\, t}\, \exp(-(y/\sqrt{4\nu\, t})^2)$ with the initial condition (5), i.e:

$$u(y,t) = \frac{u_0}{2}\left[\mathrm{Erf}\left(\frac{y+L/2}{\sqrt{4\nu\, t}}\right) - \mathrm{Erf}\left(\frac{y-L/2}{\sqrt{4\nu\, t}}\right)\right], \tag{6}$$

where, $\mathrm{Erf}(x) = 2/\sqrt{\pi}\int_0^x \exp(-t^2)\mathrm{d}t$ is the standard error function. There is only one non-zero component of vorticity is $\omega_3 = -\partial u/\partial y$, which is given by:

$$\omega_3(y,t) = \frac{-u_0}{\sqrt{4\pi\nu\, t}}\left[\mathrm{e}^{-\left(\frac{y+L/2}{\sqrt{4\nu\, t}}\right)^2} - \mathrm{e}^{-\left(\frac{y-L/2}{\sqrt{4\nu\, t}}\right)^2}\right]. \tag{7}$$

The time evolution of ω_3 shown in figure 11(a), with $\nu = 1/Re = 1/3200$, $u_0 = 1$ and $L = 1$, starting from $t = 100$ to 1000. The solution starts like two impulse functions at $\pm L/2$ and diffuses for later times.

The equation for 'enstrophy' (ω_3^2) in this case is:

$$\frac{\partial \omega_3^2}{\partial t} = \nu \frac{\partial^2 \omega_3^2}{\partial y^2} - 2\nu\left(\frac{\partial \omega_3}{\partial y}\right)^2. \tag{8}$$

Following the same procedure to obtain equation (2), the 'entrainment velocity' for the laminar case is given by:

$$v_{n-\mathrm{Lam}} = \underbrace{\frac{-\nu}{\left|\frac{\partial \omega_3^2}{\partial y}\right|}\frac{\partial^2 \omega_3^2}{\partial y^2}}_{v^{dif}_{n-\mathrm{Lam}}} + \underbrace{\frac{2\nu}{\left|\frac{\partial \omega_3^2}{\partial y}\right|}\left(\frac{\partial \omega_3}{\partial y}\right)^2}_{v^{dis}_{n-\mathrm{Lam}}}. \tag{9}$$

All the terms for $v_{n-\mathrm{Lam}}$ are exactly available through (7), and they are plotted as the ratio $v^{dif}_{n-\mathrm{Lam}}/v^{dis}_{n-\mathrm{Lam}}$ in figure 11(b). The inset shows the zoomed in view of the vertical axis about zero.

Two interesting observations can be made by comparing the laminar case in figure 11(b) and turbulent case in figure 5 (a) and (b). First, in the laminar case the inviscid component of entrainment velocity is identically zero.

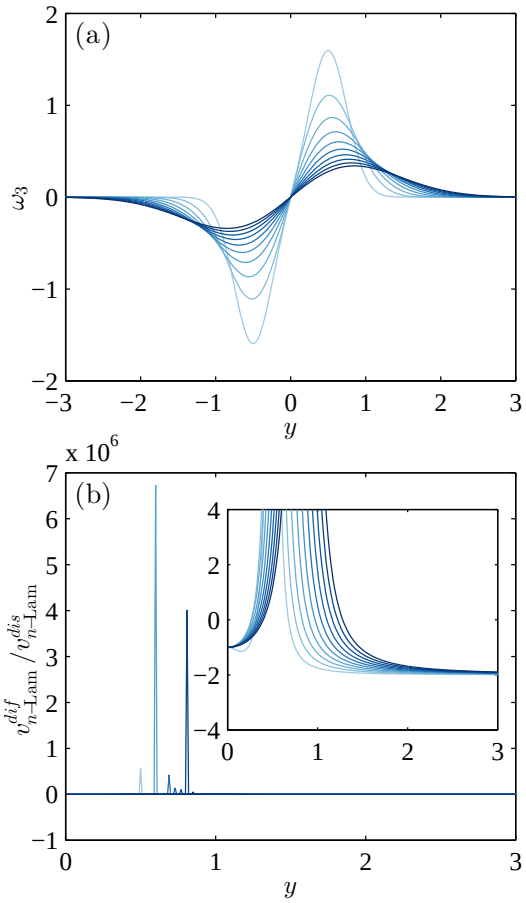

Figure 11. Laminar solution of a temporal wake for $t =$ 100 to 1000 in steps of 100. Darker lines are later times. (a) ω_3 from (7). (b) The ratio $v^{dif}_{n-\mathrm{Lam}}/v^{dis}_{n-\mathrm{Lam}}$, and the inset shows a zoomed in ordinate. Note that in (b) the maximum value of the vertical axis is 7×10^6, whereas in the inset it is 4.

This is approximately the case for $t = 500$, where the pdf for v_n^{inv} is narrow and centered around the origin. For the later times, even though the peak of the pdf for v_n^{inv} is close to zero, there are clear long tails. Note that, in the laminar case we cannot plot a pdf of v_n/u_η as in figure 5 because u_η is zero at the centerline for the laminar case due to symmetry.

Second, we notice from figure 5(b) that the ratio v_n^{dif}/v_n^{dis} is about -2 for $t = 500$ and for later times, again, the broad tails are observed. For the laminar case, in the inset of figure 11(b), we see that the ratio again tends to a value of -2. This suggests that at the 'real' TNTI a mechanism similar to the laminar case exists, where predominantly the diffusion is balancing the dissipation. This is also evident from the condition profiles shown in figure 4.

For the laminar case the ratio $v^{dif}_{n-\mathrm{Lam}}/v^{dis}_{n-\mathrm{Lam}} = -(1/2)(\partial^2\omega_3^2/\partial y^2)/(\partial\omega_3/\partial y)^2 \approx -2$ can be deduced as follows. We consider the right hand side 'boundary' of the laminar wake, i.e., $y > 0$ and $y \gg L/2$, and for physically relevant times such that $y/\sqrt{4\nu t}$ is not far from unity. For such a case,

$$\omega_3(y,t) \approx \frac{u_0}{\sqrt{4\pi\nu\, t}}\, \mathrm{e}^{-\left(\frac{y}{\sqrt{4\nu\, t}}\right)^2}, \qquad (10)$$

$$\left(\frac{\partial\omega_3}{\partial y}\right)^2 \approx \frac{u_0^2}{4\pi\nu\, t}\frac{4y^2}{(4\nu t)^2}\, \mathrm{e}^{-2\left(\frac{y}{\sqrt{4\nu\, t}}\right)^2}, \qquad (11)$$

and again, for $y \gg 0$,

$$\frac{\partial^2\omega_3^2}{\partial y^2} \approx \frac{u_0^2}{4\pi\nu\, t}\frac{(4y)^2}{(4\nu t)^2}\, \mathrm{e}^{-2\left(\frac{y}{\sqrt{4\nu\, t}}\right)^2}, \qquad (12)$$

from where it is evident that $v^{dif}_{n-\mathrm{Lam}}/v^{dis}_{n-\mathrm{Lam}} \approx -2$. We note that a different argument is given by van Reeuwijk & Holzner (2014) for $v_n^{dif}/v_n^{dis} \approx -2$, by considering that production (or v_n^{inv}) is approximately zero in the vicinity of the TNTI.

REFERENCES

Bermejo-Moreno, I. & Pullin, D. I 2008 On the non-local geometry of turbulence. *J. Fluid Mech.* **603**, 101–135.

Bisset, D. K., Hunt, J. C. R. & Rogers, M. M. 2002 The turbulent/non-turbulent interface bounding a far wake. *J. Fluid Mech.* **451**, 383–410.

Chauhan, K., Philip, J. & Marusic, I. 2014 Scaling of the turbulent/non-turbulent interface in boundary layers. *J. Fluid Mech.* **751**, 298–328.

Holzner, M. & Lüthi, B. 2011 Laminar superlayer at the turbulence boundary. *Phys. Rev. Lett.* **106**, 134503.

Koenderink, J. J. & van Doorn, A. J. 1992 Surface shape and curvature scales. *Image and vision computing* **10** (8), 557–564.

Philip, J. & Marusic, I. 2012 Large-scale eddies and their role in entrainment in turbulent jets and wakes. *Phys. Fluids* **24**, 055108.

Philip, J., Meneveau, C., de Silva, C. M. & Marusic, I. 2014 Multiscale analysis of fluxes at the turbulent/non-turbulent interface in high Reynolds number boundary layers. *Phys. Fluids* **26** (1), 015105.

van Reeuwijk, M & Holzner, M 2014 The turbulence boundary of a temporal jet. *J. Fluid Mech.* **739**, 254–275.

da Silva, C. B., Hunt, J. C. R., Eames, I. & Westerweel, J. 2014*a* Interfacial layers between regions of different turbulence intensity. *Ann. Rev. Fluid Mech.* **46** (1), 567–590.

da Silva, C. B. & Pereira, J. C. F. 2008 Invariants of the velocity-gradient, rate-of-strain, and rate-of-rotation tensors across the turbulent/nonturbulent interface in jets. *Phys. Fluids* **20** (5), 055101.

da Silva, C. B. & Taveira, R. R. 2010 The thickness of the turbulent/nonturbulent interface is equal to the radius of the large vorticity structures near the edge of the shear layer. *Phys. Fluids* **22**, 121702.

da Silva, C. B., Taveira, R. R. & Borrell, G. 2014*b* Characteristics of the turbulent/nonturbulent interface in boundary layers, jets and shear-free turbulence. *J. of Phys.: Conference Series* **506**, 012015.

Taveira, R. R., Diogo, J. S., Lopes, D. C. & da Silva, C. B. 2013 Lagrangian statistics across the turbulent-nonturbulent interface in a turbulent plane jet. *Phys. Rev. E* **88**, 043001.

Westerweel, J., Fukushima, C., Pedersen, J. M. & Hunt, J. C. R. 2005 Mechanics of the turbulent-nonturbulent interface of a jet. *Phys. Rev. Lett.* **95**, 174501.

Wolf, M., Lüthi, B., Holzner, M., Krug, D., Kinzelbach, W. & Tsinober, A. 2012 Investigations on the local entrainment velocity in a turbulent jet. *Phys. Fluids* **24**, 105110.